

## RESEARCH ARTICLE

View Article Online  
View Journal | View IssueCite this: *Inorg. Chem. Front.*, 2022,  
9, 4753Photocatalytic CO<sub>2</sub> reduction on Cu single atoms incorporated in ordered macroporous TiO<sub>2</sub> toward tunable products†Cong Chen,<sup>a</sup> Ting Wang,<sup>a</sup> Ke Yan,<sup>a</sup> Shoujie Liu,<sup>b</sup> Yu Zhao<sup>c</sup> and Benxia Li<sup>\*a</sup>

The photocatalytic conversion of CO<sub>2</sub> to hydrocarbons is a fascinating strategy to defuse the growing energy and environmental dilemmas, but there are great challenges in improving photocatalytic efficiency and tuning product selectivity. Both are of equal importance to increase the yield of the desired product and clarify the photocatalytic CO<sub>2</sub> reduction mechanism. Herein, a Cu single-atom-incorporated three-dimensional-ordered macroporous TiO<sub>2</sub> (Cu<sub>0.01</sub>/3DOM-TiO<sub>2</sub>) photocatalyst was synthesized using a template-assisted *in situ* pyrolysis method. The Cu single atoms are uniformly anchored in a 3DOM TiO<sub>2</sub> matrix, which not only broadens the light absorption range but also provides specific active sites for the adsorption and transformation of CO<sub>2</sub> molecules. The photocatalytic CO<sub>2</sub> reduction reaction was conducted in gas–solid and liquid–solid systems, respectively, to explore the effects of reaction modes on the CO<sub>2</sub> conversion efficiency and product selectivity. The results indicate that the photocatalytic CO<sub>2</sub> reduction reaction in gas–solid system mainly produces methane (CH<sub>4</sub>), with a high selectivity of 83.3% and a formation rate of 43.15 μmol g<sup>-1</sup> h<sup>-1</sup>. In contrast, the main product in the liquid–solid system is ethylene (C<sub>2</sub>H<sub>4</sub>), with a selectivity of 58.4% and a formation rate of 6.99 μmol g<sup>-1</sup> h<sup>-1</sup>. The Cu<sub>0.01</sub>/3DOM-TiO<sub>2</sub> photocatalyst shows superior activity and selectivity in the gas–solid system while favorably producing C<sub>2</sub>H<sub>4</sub> in the liquid–solid system. The possible photocatalytic mechanisms of CO<sub>2</sub> reduction in the two different reaction systems are discussed according to *in situ* infrared spectroscopy. This work provides some new information on promoting photocatalytic CO<sub>2</sub> reduction to desirable products by the rational design of photocatalysts as well as tuning the reaction conditions.

Received 29th May 2022,  
Accepted 19th July 2022

DOI: 10.1039/d2qi01155g

rsc.li/frontiers-inorganic

## 1. Introduction

Photosynthetic organisms harness solar energy to convert CO<sub>2</sub> and H<sub>2</sub>O into carbohydrates and oxygen, which achieves energy transformation in nature and maintains the carbon–oxygen balance. Enlightened by natural photosynthesis, artificial photosynthesis for CO<sub>2</sub> reduction with H<sub>2</sub>O powered by solar irradiation has attracted extensive interest, which is regarded as a double-benefit approach that converts greenhouse gas to chemical fuels and valuable chemicals by harvesting solar energy.<sup>1</sup> However, the reactivity and product selectivity

of photocatalytic CO<sub>2</sub> reduction are always restricted by three main obstacles: (1) the difficult adsorption of reactants on photocatalysts in heterogeneous catalytic systems, (2) the high energy requirement for C–O bond activation up to 750 kJ mol<sup>-1</sup>, and (3) the various intermediates and complex pathways of the CO<sub>2</sub> transformation process.<sup>2,3</sup> Hence, the rational construction of heterogeneous photocatalysts is imperative for improving the reactivity and product selectivity of CO<sub>2</sub> reduction, which requires the meticulous design and masterly integration of a light-harvesting component and catalytically active sites.<sup>4</sup>

In recent years, single-atom (SA) catalysts have emerged as new options for the design and preparation of cost-effective and high-efficiency photocatalysts, which provide 100% active metal dispersion and thus maximize metal utilization.<sup>5</sup> The SA catalysts can be designed on the atomic scale by rationally embellishing the isolated specific metal-atom sites on the support materials.<sup>6</sup> Based on the inherent functions of light absorption and photo-generated carriers supplying the support materials, SA active sites further offer catalytic centers for promoting charge separation/transfer and reactant adsorp-

<sup>a</sup>Department of Chemistry, Key Laboratory of Surface & Interface Science of Polymer Materials of Zhejiang Province, Zhejiang Sci-Tech University, Hangzhou 310018, PR China. E-mail: libx@zstu.edu.cn

<sup>b</sup>Chemistry and Chemical Engineering of Guangdong Laboratory, Shantou 515063, P. R. China

<sup>c</sup>College of Material, Chemistry and Chemical Engineering, Key Laboratory of Organosilicon Chemistry and Material Technology, Ministry of Education, Hangzhou Normal University, Hangzhou, Zhejiang 311121, PR China

† Electronic supplementary information (ESI) available. See DOI: <https://doi.org/10.1039/d2qi01155g>

tion/activation.<sup>7</sup> Moreover, the definite active centers of SA photocatalysts enable improved understanding of the fundamental mechanism of photocatalysis, and allow us to draw more precise structure–performance correlations. Therefore, various metal cocatalysts including noble metals, transition metals and rare Earth metals, have been prepared in SA sites to increase the photocatalytic efficiency.<sup>8–12</sup> Among them, copper (Cu) has been identified as one of the most promising cocatalysts to convert CO<sub>2</sub> into various hydrocarbons owing to its optimum binding ability with CO<sub>2</sub> and reaction intermediates.<sup>13–16</sup> The individual Cu atoms immobilized on light-harvesting semiconductors can act as excellent active sites for activating CO<sub>2</sub> molecules and stabilizing reaction intermediates in the photocatalytic CO<sub>2</sub> reduction reaction.<sup>17,18</sup> Moreover, the introduction of highly dispersed Cu heteroatoms in light-harvesting semiconductors can broaden the light-adsorption range and enhance the photo-excited charge separation efficiency.<sup>19</sup> Although numerous studies have highlighted the excellent catalytic activity of Cu SAs in electrocatalytic/photocatalytic CO<sub>2</sub> reduction,<sup>16,20,21</sup> the controllable and large-scale production of heterogeneous photocatalysts with Cu SAs is still challenging. Most strategies to anchor Cu SAs on light-harvesting semiconductors are explored as post-treatment methods (*e.g.* impregnation and photodeposition), where the Cu SAs tend to aggregate into nanoparticles or leach from supports during photocatalytic reactions because of the weak combination.<sup>22,23</sup> Hence, the *in situ* incorporation of highly stable Cu SAs in semiconductors is desirable. Meanwhile, the morphological features of the semiconductor support are a crucial factor to create stable Cu single atoms as well as heterogeneous photocatalysts with high performance, where the support not only determines the availability and stability of Cu SA sites but also supplies photogenerated electrons for CO<sub>2</sub> reduction. Three-dimensional ordered macroporous (3DOM) materials with an interpenetrating porous structure and high porosity can greatly facilitate CO<sub>2</sub> diffusion and enhance the light utilization simultaneously.<sup>24,25</sup> Moreover, the large specific surface area of the 3DOM support can afford more accessible Cu SA sites for CO<sub>2</sub> photoreduction.<sup>26</sup> Although some metal-modified 3DOM TiO<sub>2</sub> photocatalysts have been reported, the formation of metal nanoparticles with large sizes generally results in limited photocatalysis.<sup>27,28</sup> Our recent study indicated that Pd single atoms could be *in situ* anchored in 3DOM CeO<sub>2</sub> *via* a template-assisted pyrolysis method owing to the strong metal–support interaction.<sup>29</sup> Inspired by this, the masterly integration of catalytically active sites (Cu SAs) and a light-harvesting semiconductor (3DOM TiO<sub>2</sub>) is expected to achieve.

In addition, tuning the selectivity of CO<sub>2</sub> reduction reaction to the desired product is of great significance but remains a huge challenge.<sup>30,31</sup> Tan and coworkers found that the ethylene selectivity of electrocatalytic CO<sub>2</sub> reduction with the same catalyst could be tuned by modulating the local CO<sub>2</sub> concentration, where the kinetics of CO<sub>2</sub> reduction was substantially influenced by the modulation of CO<sub>2</sub> mass transport.<sup>32</sup> Wang

*et al.* reported that the introduction of N<sub>2</sub> into CO<sub>2</sub> could control the \*CO coverage on Cu–Au bimetallic catalysts and thus facilitate \*CO protonation for methane formation.<sup>33</sup> However, the effects of reaction conditions on product selectivity of CO<sub>2</sub> photoreduction are rarely studied. The photocatalytic CO<sub>2</sub> reduction reaction is commonly conducted in either a liquid–solid or a gas–solid system. Actually, the reaction system is a non-negligible factor influencing the product selectivity of CO<sub>2</sub> photoreduction. Therefore, exploring the effect of reaction systems on the product selectivity of photocatalytic CO<sub>2</sub> reduction is as important as the development of efficient photocatalysts. In this work, a heterogeneous photocatalyst of 3DOM TiO<sub>2</sub> doped with Cu single atoms (Cu<sub>0.01</sub>/3DOM-TiO<sub>2</sub>) is controllably synthesized *via* a facile template-assisted pyrolysis method. Taking this catalyst as a research model, the photocatalytic CO<sub>2</sub> reduction performance is studied in gas–solid and liquid–solid reaction systems, respectively, to explore the effects of reaction modes on the catalytic activity and product selectivity. Interestingly, the Cu<sub>0.01</sub>/3DOM-TiO<sub>2</sub> photocatalyst exhibits higher activity and selectivity for methane (CH<sub>4</sub>) production in the gas–solid system, while possessing a favorable capability to convert CO<sub>2</sub> into ethylene (C<sub>2</sub>H<sub>4</sub>) in the liquid–solid system. The possible photocatalytic mechanisms of CO<sub>2</sub> reduction in both catalytic systems are discussed according to *in situ* diffused reflection infrared Fourier transform spectroscopy (DRIFTS) measurements.

## 2. Experimental

### 2.1. Chemicals

Titanium butoxide (C<sub>16</sub>H<sub>36</sub>O<sub>4</sub>Ti, ≥99.0%), anhydrous cupric chloride (CuCl<sub>2</sub>, 98%), styrene (>99.5%, GC), potassium persulfate (K<sub>2</sub>S<sub>2</sub>O<sub>8</sub>, AR, 99.5%), sodium hydroxide (NaOH, 97%), acetic acid glacial (CH<sub>3</sub>COOH, ≥99.8%), ethanol (CH<sub>3</sub>CH<sub>2</sub>OH, ≥99.7%), methanol (CH<sub>3</sub>OH, 99.5%), sodium sulfate anhydrous (Na<sub>2</sub>SO<sub>4</sub>, 99%), potassium iodide (KI, 99%), potassium hydrogen phthalate (C<sub>8</sub>H<sub>5</sub>KO<sub>4</sub>, 99.8%), N<sub>2</sub> (≥99.99%), CO<sub>2</sub> (≥99.99%) and argon gas (≥99.99%) were obtained commercially and used without further purification.

### 2.2. Synthesis of Cu/3DOM-TiO<sub>2</sub> photocatalysts

Firstly, the monodisperse polystyrene (PS) sub-microspheres with diameters of about 260 nm were prepared using an emulsifier-free emulsion polymerization process and assembled into the PS colloidal crystal templates (CCTs) by centrifugation.<sup>29</sup> The as-prepared CCTs were immersed in methanol for 30 min and then dried for a moment to remove the superfluous methanol. Subsequently, the Cu/3DOM-TiO<sub>2</sub> photocatalysts were prepared using a template-assisted pyrolysis method. Specifically, methanol (0.5 mL), acetic acid glacial (0.5 mL), titanium butoxide (2.72 g) and a certain amount of CuCl<sub>2</sub> were mixed by vigorous stirring for 2 h to form a homogeneous precursor solution. The pretreated CCTs were immersed in the precursor solution under vacuum treatment.

After being subjected to a vacuum for 1 h, the CCTs impregnated with precursor solution were collected, dried at room temperature, and calcined in air at 550 °C for 3 h (heating rate 1 °C min<sup>-1</sup>) to obtain the Cu/3DOM-TiO<sub>2</sub> photocatalysts. The Cu content in the Cu/3DOM-TiO<sub>2</sub> photocatalysts was adjusted by changing the dosage of CuCl<sub>2</sub>, and the as-synthesized photocatalyst was denoted as Cu<sub>x</sub>/3DOM-TiO<sub>2</sub>, where *x* represents the molar ratio of Cu to Ti based on the dosages of CuCl<sub>2</sub> and titanium butoxide. For example, the Cu<sub>0.01</sub>/3DOM-TiO<sub>2</sub> photocatalyst was prepared by adding 10.8 mg CuCl<sub>2</sub> to the precursor solution. In addition, the other Cu<sub>x</sub>/3DOM-TiO<sub>2</sub> samples (*x* = 0.0075, 0.0125, 0.02, 0.03, 0.04 and 0.05) were also synthesized by adding the corresponding dosage of CuCl<sub>2</sub>. The actual Cu contents of Cu<sub>0.0075</sub>/3DOM-TiO<sub>2</sub>, Cu<sub>0.01</sub>/3DOM-TiO<sub>2</sub>, Cu<sub>0.0125</sub>/3DOM-TiO<sub>2</sub>, Cu<sub>0.02</sub>/3DOM-TiO<sub>2</sub>, Cu<sub>0.03</sub>/3DOM-TiO<sub>2</sub>, Cu<sub>0.04</sub>/3DOM-TiO<sub>2</sub> and Cu<sub>0.05</sub>/3DOM-TiO<sub>2</sub> were measured by atomic absorption spectroscopy (AAS) as 0.51 wt%, 0.69 wt%, 1.03 wt%, 1.33 wt%, 1.98 wt%, 2.75 wt% and 3.38 wt%, respectively.

### 2.3. Synthesis of control samples

Several control samples including 3DOM-TiO<sub>2</sub>, Cu<sub>0.01</sub>/TiO<sub>2</sub> and TiO<sub>2</sub> were prepared using a similar procedure to that for preparing the Cu<sub>0.01</sub>/3DOM-TiO<sub>2</sub> photocatalyst, without adding CuCl<sub>2</sub>, CCTs, CuCl<sub>2</sub> and CCTs, respectively.

### 2.4. Characterization

The crystalline components of photocatalysts were analyzed using a powder X-ray diffractometer (XRD, DX-2700) with Cu K $\alpha$  radiation. The actual Cu contents of the Cu<sub>x</sub>/3DOM-TiO<sub>2</sub> photocatalysts were measured on an atomic absorption spectrophotometer (Shimadzu AA-7000). The microstructures were observed using field emission scanning electron microscopy (FESEM, ZEISS Ultra-55) operated at 3.0 kV and transmission electron microscopy (TEM, JEOL-2010) working at 200 kV. Nitrogen adsorption/desorption isotherms were recorded on a Micromeritics ASAP 2460 apparatus at 77 K, to determine the specific surface areas and the pore size distributions of the photocatalysts. Thermogravimetric (TG) analysis was performed on a thermal gravimetric analyzer (TG209F3 Tarsus, Netzsch). Raman spectra were acquired on a Horiba Scientific LabRAM HR Evolution apparatus with a 514 nm laser as the excitation source. X-ray photoelectron spectra (XPS) were measured using a Thermo Scientific K-Alpha X-ray photoelectron spectrometer, and the binding energies were calibrated with a C 1s peak at 284.8 eV as the reference. UV-vis diffuse reflectance spectra (DRS) were taken on a Shimadzu UV-2600 spectrophotometer with BaSO<sub>4</sub> as the reference. Photoluminescence (PL) spectra were measured on a HORIBA Fluoromax-4 spectrophotometer at an excitation wavelength of 350 nm. The radical intermediates generated during photocatalytic CO<sub>2</sub> reduction were detected using *in situ* electron spin resonance (ESR) on a Bruker model JEOL JES-FA200 spectrometer, with 5,5-dimethyl-1-pyrroline-*N*-oxide (DMPO) as a radical-trapping reagent. The X-ray absorption of fine structures (XAFS) measurements of the Cu K-edge were conducted

at the BL14W1 station at the Shanghai Synchrotron Radiation Facility (SSRF), China. The spectra were recorded in fluorescent mode using a Si (311) double-crystal monochromator and a 32-element Ge solid-state detector. The electron storage ring was operated at 3.5 GeV. Cu foil and CuO were employed as the reference samples. The XAFS data were processed using Athena and Artemis software, according to the standard procedures.

### 2.5. Photocatalytic CO<sub>2</sub> reduction tests

The photocatalytic CO<sub>2</sub> reduction reactions were carried out in a top-irradiated reactor with a volume of 170 mL. The simulated sunlight with a main irradiation range of 320–780 nm was provided by a Xe lamp (PLS-SXE300, Beijing Perfectlight) equipped with a specific reflector, and the optical power density irradiated on the reaction solution was 200 mW cm<sup>-2</sup>. The photocatalytic CO<sub>2</sub> reduction reaction was conducted in gas–solid and liquid–solid systems, respectively. For the gas–solid reaction mode, the slurry prepared by dispersing 5 mg photocatalyst in 1 mL ethanol was coated on a glass plate (2 × 2 cm) and then dried at 60 °C. The glass-supported photocatalyst was placed at the bottom of the reactor, and 1 mL of deionized water was dripped beside the glass plate. After CO<sub>2</sub> gas was blown into the reactor and absorption equilibrium was achieved in dark, the photocatalytic CO<sub>2</sub> reduction reaction was started under simulated sunlight. For the liquid–solid reaction mode, the reaction suspension containing 5 mg of photocatalyst and 30 mL of water was transformed in the reactor, which was bubbled with CO<sub>2</sub> gas for 20 min. After the sealed reactor had been kept in dark for 30 min, the photocatalytic CO<sub>2</sub> reduction reaction was started under simulated sunlight from a Xe lamp. The photocatalytic reactions were conducted for 4 h to obtain the average generation rates of products. The gas products (CO, CH<sub>4</sub>, C<sub>2</sub>H<sub>4</sub>) were quantitatively analyzed using a gas chromatograph (GC 9790 II, FuLi) equipped with both a thermal conductivity detector (TCD) and a flame ionization detector (FID). The liquid products were identified using <sup>1</sup>H nuclear magnetic resonance (NMR) spectrometry in D<sub>2</sub>O, which was performed on a Bruker AVANCE AV 400 MHz spectrometer. For the recycling experiments, the reaction system was re-blown or re-bubbled with CO<sub>2</sub> gas after each reaction cycle and then irradiated for the next reaction cycle.

### 2.6. *In situ* DRIFTS measurement

The *in situ* diffused reflection infrared Fourier transform spectroscopy (DRIFTS) analysis was performed on a Bruker TENSOR II FTIR spectrometer equipped with a mercury-cadmium-tellurium (MCT) detector cooled with liquid nitrogen. For the gas–solid reaction mode, 30 mg of the photocatalyst was placed in the test chamber, which was then subjected to a vacuum. After the background spectrum was collected from 400 to 4000 cm<sup>-1</sup>, humid CO<sub>2</sub> gas was introduced into the test chamber to achieve adsorption–desorption equilibrium in the dark for 30 min. Subsequently, the time-dependent DRIFTS spectra were recorded upon irradiation from the Xe lamp. For the liquid–solid reaction mode, the operations

were the same as those described above, except that a drop of deionized water was dripped beside the photocatalyst on the sample holder.

### 3. Results and discussion

#### 3.1. Structures and properties of photocatalysts

The  $\text{Cu}_x/3\text{DOM-TiO}_2$  photocatalysts were synthesized *via* a template-assisted pyrolysis method as illustrated in Fig. 1a. The monodisperse PS sub-microspheres were assembled into colloidal crystal templates which were impregnated with the precursor solution containing  $\text{Cu}^{2+}$  ions and titanium butoxide. The  $\text{Cu}_x/3\text{DOM-TiO}_2$  photocatalysts with different Cu contents were obtained *via* calcination of the colloidal crystal templates loaded with precursors in air at 550 °C for 3 h. The thermogravimetric (TG) analysis (Fig. S1, ESI†) indicated that the PS-sphere template decomposes at 400 °C in air and the precursors are completely converted into the final material below 500 °C. Therefore, it is reasonable to conduct the calcination at 550 °C for 3 h, during which the individual Cu single atoms are *in situ* anchored in the 3DOM- $\text{TiO}_2$  matrix. The XRD patterns of the typical  $\text{Cu}_{0.01}/3\text{DOM-TiO}_2$  photocatalyst and the control samples (3DOM- $\text{TiO}_2$ ,  $\text{Cu}_{0.01}/\text{TiO}_2$  and  $\text{TiO}_2$ ) are shown in Fig. 1b. The photocatalysts obtained from the template-assisted synthesis ( $\text{Cu}_{0.01}/3\text{DOM-TiO}_2$  and 3DOM- $\text{TiO}_2$ ) consist

of anatase  $\text{TiO}_2$  (JCPDS no. 01-562) accompanied by a small quantity of rutile  $\text{TiO}_2$  (JCPDS no. 01-1292), while the  $\text{Cu}_{0.01}/\text{TiO}_2$  and  $\text{TiO}_2$  samples synthesized by the direct pyrolysis of precursors without the PS template present only the diffraction peaks of anatase  $\text{TiO}_2$ . The mass fractions of rutile  $\text{TiO}_2$  ( $W_{\text{Rutile}}$ ) in  $\text{Cu}_{0.01}/3\text{DOM-TiO}_2$  and 3DOM- $\text{TiO}_2$  are estimated to be 13.86 wt% and 13.80 wt%, respectively, according to the previously reported formula:<sup>34,35</sup>  $W_{\text{Rutile}} = A_{\text{Rutile}} / (0.884 A_{\text{Anatase}} + A_{\text{Rutile}})$ , where  $A_{\text{Anatase}}$  and  $A_{\text{Rutile}}$  are the integrated intensities of the anatase (101) and rutile (110) XRD peaks. The previous study demonstrated that the calcination process assisted by a PS colloidal crystal template could produce mixed phases of anatase and rutile.<sup>27</sup> As a light-harvesting material,  $\text{TiO}_2$  containing both anatase and rutile phases is desirable because the anatase/rutile junction facilitates spatial charge separation, allowing more photogenerated charge carriers to migrate to the surface and participate in redox reactions.<sup>36</sup> The diffraction peaks of Cu species are not observed in the XRD patterns of both the  $\text{Cu}_{0.01}/3\text{DOM-TiO}_2$  and the  $\text{Cu}_{0.01}/\text{TiO}_2$  samples due to the high dispersity and/or low content of Cu. Compared with  $\text{TiO}_2$  and 3DOM- $\text{TiO}_2$ , the typical diffraction peaks of  $\text{Cu}_{0.01}/3\text{DOM-TiO}_2$  and  $\text{Cu}_{0.01}/\text{TiO}_2$  present obvious shifts to lower  $2\theta$  positions (Fig. S2, ESI†), which are caused by the doping of Cu cations with larger ionic radii ( $\text{Cu}^{2+}$ , 0.73 Å;  $\text{Cu}^+$ , 0.77 Å; and  $\text{Ti}^{4+}$ , 0.61 Å) into  $\text{TiO}_2$ .<sup>37,38</sup> In addition, the anatase (101) diffraction peak of  $\text{Cu}_{0.01}/3\text{DOM-TiO}_2$  and 3DOM- $\text{TiO}_2$

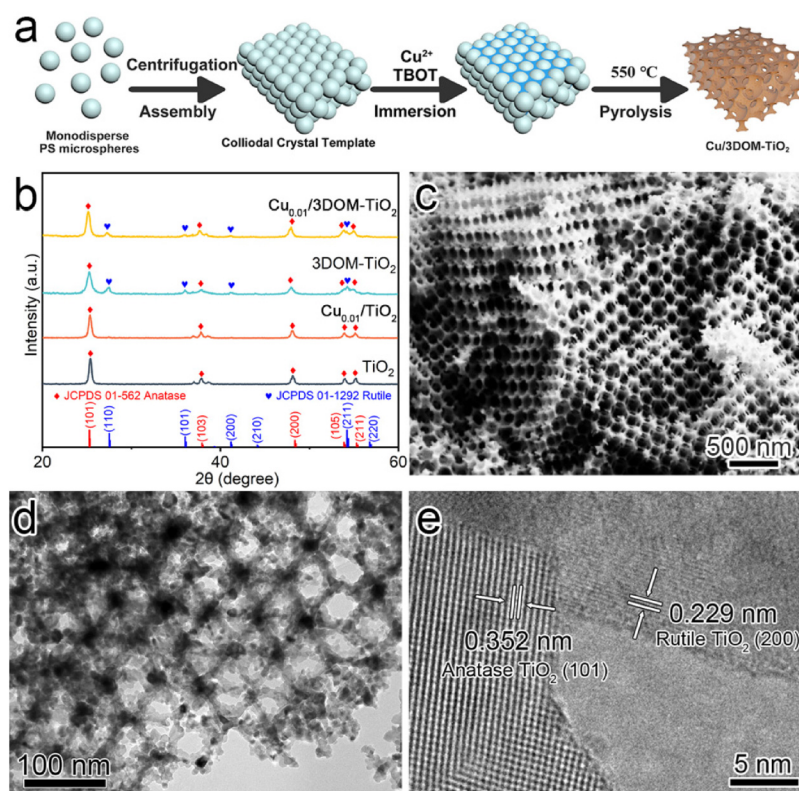


**Fig. 1** (a) Schematic diagram of the synthesis of  $\text{Cu}_{0.01}/3\text{DOM-TiO}_2$  photocatalyst. (b) XRD patterns of different samples; (c) SEM, (d) TEM and (e) HRTEM images of  $\text{Cu}_{0.01}/3\text{DOM-TiO}_2$ .

presents further shifts towards lower  $2\theta$  positions compared with those of  $\text{Cu}_{0.01}/\text{TiO}_2$  and  $\text{TiO}_2$ , possibly because the special 3DOM structures result in little lattice distortion.<sup>39,40</sup> The SEM images (Fig. 1c; Fig. S3a, ESI†) affirm that the  $\text{Cu}_{0.01}/3\text{DOM-TiO}_2$  photocatalyst exhibits a honeycomb morphology with 3D ordered macroporous structures, where the spherical voids have an average diameter of 160 nm and the walls have an average thickness of about 10 nm. These spherical voids are well arranged and interconnected. The 3DOM- $\text{TiO}_2$  sample (Fig. S3b, ESI†) presents a similar honeycombed morphology to that of the  $\text{Cu}_{0.01}/3\text{DOM-TiO}_2$  photocatalyst. In contrast,  $\text{Cu}_{0.01}/\text{TiO}_2$  (Fig. S3c, ESI†) and  $\text{TiO}_2$  (Fig. S3d, ESI†) synthesized by the direct pyrolysis of precursors without a PS template are irregular bulks without porosity. The TEM image shown in Fig. 1d indicates that the 3DOM frameworks are constructed from numerous  $\text{TiO}_2$  small particles. The HRTEM image (Fig. 1e) reveals the crystalline phase boundary of anatase and rutile, where the characteristic spacings of 0.352 and 0.229 nm are assignable to the (101) lattice of anatase  $\text{TiO}_2$  and the (200) lattice of rutile  $\text{TiO}_2$ , respectively. The crystalline lattices of  $\text{CuO}$  or  $\text{Cu}_2\text{O}$  are not found in the HRTEM image of  $\text{Cu}_{0.01}/3\text{DOM-TiO}_2$ , suggesting that Cu element exists as highly dispersed species in this material.

The specific surface areas and pore size distributions of  $\text{Cu}_{0.01}/3\text{DOM-TiO}_2$ , 3DOM- $\text{TiO}_2$  and  $\text{Cu}_{0.01}/\text{TiO}_2$  were determined using  $\text{N}_2$  adsorption–desorption measurements (Fig. 2; Fig. S4, ESI†). Both  $\text{Cu}_{0.01}/3\text{DOM-TiO}_2$  and 3DOM- $\text{TiO}_2$  samples display the typical type IV isotherm with a hysteresis loop, and the dominant adsorption of both samples can be identified as macropores corresponding to the step at  $P/P_0 = 0.8–0.995$  (Fig. 2a).<sup>41</sup> In contrast,  $\text{Cu}_{0.01}/\text{TiO}_2$  presents an extremely weak  $\text{N}_2$  adsorption capacity (Fig. S4, ESI†) due to its large bulk morphology without porosity.  $\text{Cu}_{0.01}/3\text{DOM-TiO}_2$  presents a specific surface area of  $52.80 \text{ m}^2 \text{ g}^{-1}$  and a pore volume of  $0.28 \text{ cm}^3 \text{ g}^{-1}$ , which are higher than those of 3DOM- $\text{TiO}_2$  (Table S2, ESI†). The  $\text{Cu}_{0.01}/\text{TiO}_2$  sample shows a

very low specific surface area ( $3.74 \text{ m}^2 \text{ g}^{-1}$ ) and a negligible pore volume ( $0.0014 \text{ cm}^3 \text{ g}^{-1}$ ). The large surface area and pore volume of  $\text{Cu}_{0.01}/3\text{DOM-TiO}_2$  are conducive to the sufficient exposure of active sites and the easy diffusion of  $\text{CO}_2$  and  $\text{H}_2\text{O}$  molecules during the photocatalytic  $\text{CO}_2$  reduction reaction.<sup>42</sup>

The Raman spectroscopy analysis shed light on the variations in local structures of  $\text{TiO}_2$  in different photocatalysts. As shown in Fig. 3a, the Raman spectra of the three samples ( $\text{Cu}_{0.01}/3\text{DOM-TiO}_2$ , 3DOM- $\text{TiO}_2$  and  $\text{Cu}_{0.01}/\text{TiO}_2$ ) exhibit five representative peaks of anatase  $\text{TiO}_2$ , which can be ascribed to the  $E_{g(1)}$ ,  $E_{g(2)}$  and  $E_{g(3)}$  modes ( $144$ ,  $197$  and  $639 \text{ cm}^{-1}$ ), the  $B_{1g}$  mode ( $397 \text{ cm}^{-1}$ ) and the doublet of the  $A_{1g}/B_{1g}$  mode ( $517 \text{ cm}^{-1}$ ), respectively.<sup>41,43</sup> Compared with  $\text{Cu}_{0.01}/\text{TiO}_2$ , 3DOM- $\text{TiO}_2$  shows a slight shift and broadening in the characteristic  $A_{1g}$  and  $B_{1g}$  vibration peaks due to the increased structural disorder resulting from the formation of the 3DOM structure.  $\text{Cu}_{0.01}/3\text{DOM-TiO}_2$  presents further broadening of the characteristic peaks because of Cu doping in 3DOM  $\text{TiO}_2$ , but no peaks of copper oxide or copper hydroxide are observed. Moreover, both 3DOM- $\text{TiO}_2$  and  $\text{Cu}_{0.01}/3\text{DOM-TiO}_2$  show a weak peak at  $448 \text{ cm}^{-1}$  (inset in Fig. 3a), which corresponds to a characteristic vibration mode of rutile  $\text{TiO}_2$ , further confirming the coexistence of the anatase and rutile phases in the two samples.<sup>44</sup> The XPS technique was employed to acquire information on the surface elemental compositions and chemical states of the photocatalysts. For the three samples ( $\text{Cu}_{0.01}/3\text{DOM-TiO}_2$ , 3DOM- $\text{TiO}_2$  and  $\text{Cu}_{0.01}/\text{TiO}_2$ ), each of the Ti 2p spectra (Fig. 3b) shows two characteristic peaks at binding energies of 458.6 and 464.3 eV, which are assignable to Ti  $2p_{3/2}$  and  $2p_{1/2}$  of  $\text{Ti}^{4+}$ , respectively.<sup>45,46</sup> Compared with  $\text{Cu}_{0.01}/\text{TiO}_2$ , the Ti  $2p_{3/2}$  and  $2p_{1/2}$  peaks of both 3DOM- $\text{TiO}_2$  and  $\text{Cu}_{0.01}/3\text{DOM-TiO}_2$  present a 0.1 eV positive shift, which is probably caused by the lattice distortions of 3DOM- $\text{TiO}_2$ .<sup>47</sup> Two peaks are deconvoluted from each O 1s spectrum (Fig. 3c), where the main peak around 529.8 eV is assigned to

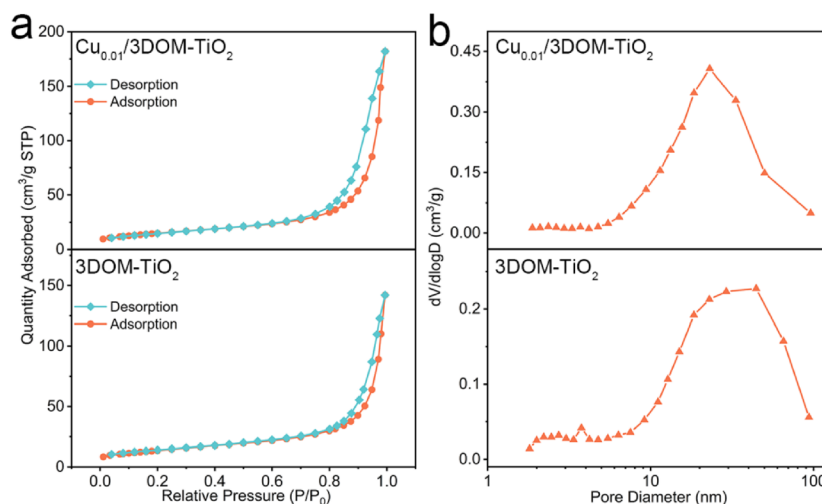
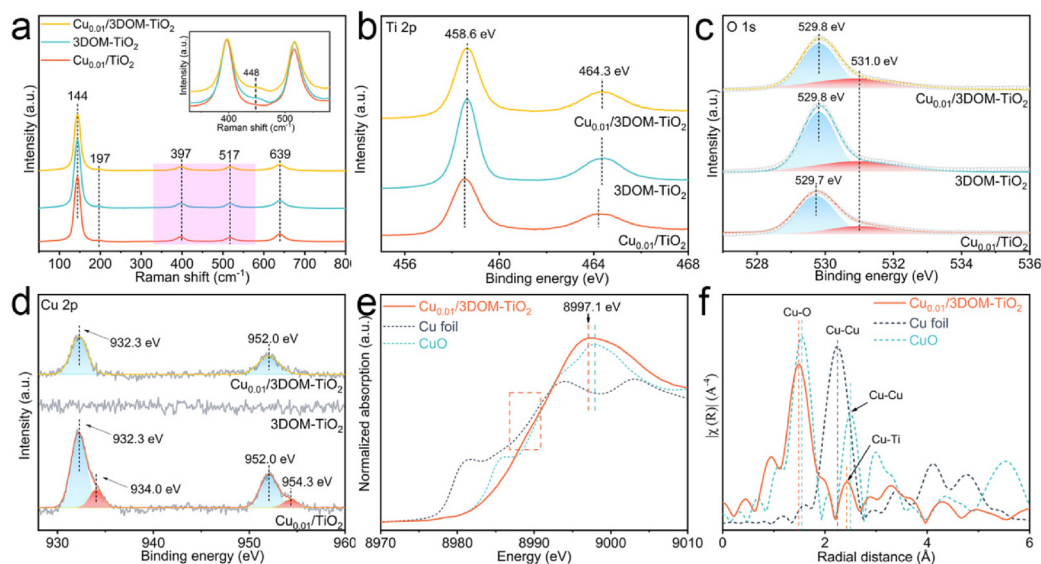


Fig. 2 (a)  $\text{N}_2$  adsorption–desorption isotherms and (b) pore size distribution plots of  $\text{Cu}_{0.01}/3\text{DOM-TiO}_2$  and 3DOM- $\text{TiO}_2$ .



**Fig. 3** (a) Raman spectra of different photocatalysts. XPS spectra of (b) Ti 2p, (c) O 1s, and (d) Cu 2p of different photocatalysts. (e) Cu K-edge XANES and (f) EXAFS spectra of  $\text{Cu}_{0.01}/3\text{DOM-TiO}_2$  with the reference samples of Cu foil and CuO.

the lattice oxygen of  $\text{TiO}_2$  and the minor peak around 531.0 eV is attributed to the surface chemisorbed oxygen on oxygen-vacancy ( $\text{V}_\text{O}$ ) sites.<sup>48–50</sup>  $\text{Cu}_{0.01}/3\text{DOM-TiO}_2$  and  $3\text{DOM-TiO}_2$  have higher oxygen-vacancy contents (34.63% and 30.74%) than  $\text{Cu}_{0.01}/\text{TiO}_2$  (24.87%), because the high specific surface area of  $3\text{DOM-TiO}_2$  exposes more surface Ti sites with unsaturated coordination.<sup>51</sup> In Fig. 3d, two characteristic peaks centered at binding energies of 932.3 and 952.0 eV appear in the Cu 2p spectra of both  $\text{Cu}_{0.01}/3\text{DOM-TiO}_2$  and  $\text{Cu}_{0.01}/\text{TiO}_2$ , which are approximate to the  $\text{Cu } 2\text{p}_{3/2}$  and  $2\text{p}_{1/2}$  of  $\text{Cu}^+$  ions,<sup>52,53</sup> indicating that the Cu single atoms incorporated in  $\text{TiO}_2$  have an electronic state close to that of the  $\text{Cu}^+$  cation. In addition, another pair of minor peaks centered at 934.0 and 954.3 eV deconvoluted from the Cu 2p spectrum of  $\text{Cu}_{0.01}/\text{TiO}_2$  can be assigned to a  $\text{Cu}^{2+}$  cation with a higher oxidation state, probably due to the formation of CuO clusters.<sup>54,55</sup> Compared with  $3\text{DOM-TiO}_2$ , the lack of peak shifts in the XPS spectra of  $\text{Cu}_{0.01}/3\text{DOM-TiO}_2$  may be ascribable to the formation of the atomically dispersed  $\text{Cu}^{\delta+}$  in the lattice of  $3\text{DOM-TiO}_2$  during the high-temperature calcination process as well as the low Cu content. Furthermore, the electronic structure and local coordination environment of Cu atoms in the  $\text{Cu}_{0.01}/3\text{DOM-TiO}_2$  photocatalyst were studied using X-ray absorption fine structure (XAFS) analysis, in comparison with Cu foil and CuO. Fig. 3e shows the normalized Cu K-edge X-ray absorption near-edge structure (XANES) spectra, where the adsorption edge of  $\text{Cu}_{0.01}/3\text{DOM-TiO}_2$  is located between those of Cu foil and CuO, indicating that the electronic state of Cu in  $\text{Cu}_{0.01}/3\text{DOM-TiO}_2$  lies between those of  $\text{Cu}^0$  and  $\text{Cu}^{2+}$ .<sup>52</sup> The adsorption peak of  $\text{Cu}_{0.01}/3\text{DOM-TiO}_2$  is centered at 8997.1 eV and shifts a little to a lower energy compared with CuO, meaning a higher electron density of Cu single atoms in this photocatalyst than for  $\text{Cu}^{2+}$  in CuO.<sup>56</sup> The coordination configura-

tion of Cu atoms in  $\text{Cu}_{0.01}/3\text{DOM-TiO}_2$  is further revealed by the extended X-ray adsorption fine structure (EXAFS) spectrum (Fig. 3f). The Cu K-edge EXAFS spectrum of  $\text{Cu}_{0.01}/3\text{DOM-TiO}_2$  presents two characteristic distances. The major peak centered at 1.4 Å corresponds to the direct binding of Cu atoms with lattice oxygen (Cu–O), while the minor peak located at 2.4 Å is assignable to Cu–Ti coordination in the  $\text{TiO}_2$  environment.<sup>57</sup> No peak of Cu–Cu metallic binding is observed, indicating that the Cu atoms are individually doped into the lattice of  $\text{TiO}_2$  and atomically distributed in the  $3\text{DOM-TiO}_2$  support.

High light-harvesting and charge separation efficiencies are fundamental requirements for efficient photocatalysis. The photoabsorption properties of bulk  $\text{TiO}_2$ ,  $3\text{DOM-TiO}_2$ ,  $\text{Cu}_{0.01}/\text{TiO}_2$  and  $\text{Cu}_{0.01}/3\text{DOM-TiO}_2$  were measured using UV–vis diffuse reflectance spectroscopy (UV–vis DRS), as shown in Fig. 4a. The bulk  $\text{TiO}_2$  shows absorption only in the ultraviolet region ( $\lambda < 400$  nm) corresponding to the intrinsic transition from valence band (VB) to conduction band (CB).  $3\text{DOM-TiO}_2$  exhibits a great enhancement in its ultraviolet-harvesting ability owing to the unique 3DOM structure as well as additional absorption from 400 nm to longer wavelengths due to the formation of more oxygen vacancies.<sup>58</sup> With the introduction of Cu atoms, the photoabsorption above 400 nm becomes more conspicuous, suggesting the presence of more  $\text{V}_\text{O}$  defect states in  $\text{TiO}_2$ .<sup>19</sup> Moreover, the Cu-incorporated  $\text{TiO}_2$  samples ( $\text{Cu}_{0.01}/\text{TiO}_2$  and  $\text{Cu}_{0.01}/3\text{DOM-TiO}_2$ ) exhibit a near-infrared absorption band near 800 nm, corresponding to d–d transitions of the dopant Cu cations.<sup>59</sup> For  $\text{Cu}_{0.01}/\text{TiO}_2$ , the photoabsorption decreases in the ultraviolet region while increasing greatly in the visible region, which is attributable to the formation of CuO on  $\text{TiO}_2$ . Photographs of the different photocatalysts are provided in Fig. 4a and Fig. S12 (ESI<sup>†</sup>), respectively. Typically, the  $\text{Cu}_{0.01}/3\text{DOM-TiO}_2$  photocatalyst is

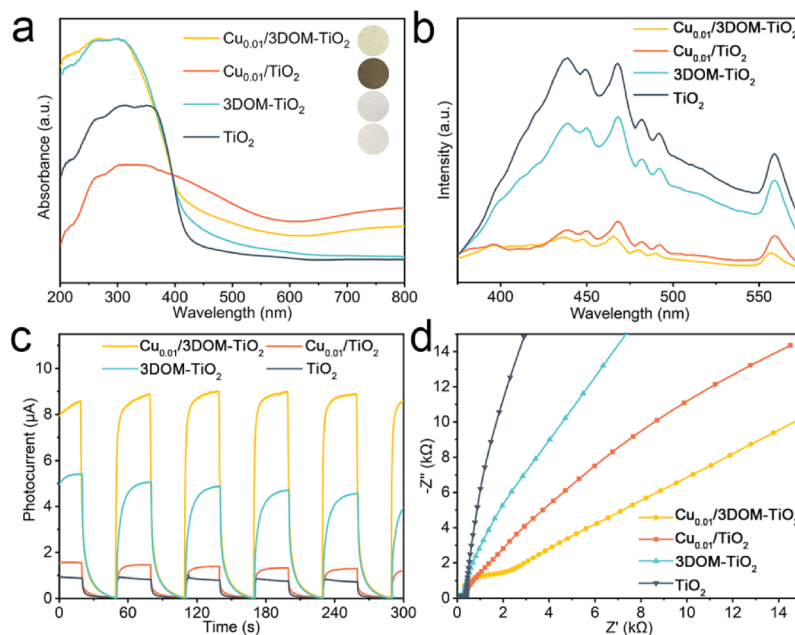


**Fig. 4** (a) Kubelka–Munk transformed UV–vis absorption spectra, (b) photoluminescence spectra, (c) transient photocurrent responses, (d) electrochemical impedance spectra of different photocatalysts.

light yellow while the  $\text{Cu}_{0.01}/\text{TiO}_2$  sample is dark green. The color of the  $\text{Cu}_x/3\text{DOM-TiO}_2$  photocatalysts changes from light yellow to brown as the Cu content increases gradually (Fig. S12, ESI†). Photoluminescence (PL) spectroscopy is employed to evaluate the separation efficiency of the photo-generated electron–hole pairs under excitation of 300 nm. The  $\text{Cu}_{0.01}/3\text{DOM-TiO}_2$  photocatalyst exhibits the weakest PL emission (Fig. 4b), suggesting the most efficient separation of photogenerated charge carriers.<sup>60</sup> The photocurrent responses and electrochemical impedance spectra (EIS) of photocatalysts were measured to further verify their photoexcited charge separation and transfer efficiencies. As shown in Fig. 4c,  $\text{Cu}_{0.01}/3\text{DOM-TiO}_2$  shows the highest photocurrent response with a light on/off mode, reflecting the most efficient separation and transfer of photoexcited charge carriers. The EIS Nyquist plot of  $\text{Cu}_{0.01}/3\text{DOM-TiO}_2$  presents the smallest arc radius (Fig. 4d), corresponding to the fastest charge transfer. These results demonstrate that the incorporation of Cu single atoms into 3DOM- $\text{TiO}_2$  affords outstanding superiority in enhancing light absorption and photogenerated charge separation/transfer efficiency. The highly dispersed Cu single-atom incorporation in  $\text{TiO}_2$  enables efficient electron transfer *via* the  $\text{Cu}^+-\text{Cu}^{2+}$  shift.<sup>22</sup> The unique structure and properties of  $\text{Cu}_{0.01}/3\text{DOM-TiO}_2$  make it a fascinating photocatalyst for  $\text{CO}_2$  conversion.

### 3.2. Photocatalytic $\text{CO}_2$ reduction performance

Two typical heterogeneous photocatalytic reaction systems of gas–solid and liquid–solid modes were employed to evaluate the performance of the  $\text{Cu}_{0.01}/3\text{DOM-TiO}_2$  photocatalyst toward  $\text{CO}_2$  reduction with water under simulated sunlight.

The effect of the Cu content in  $\text{Cu}_{0.01}/3\text{DOM-TiO}_2$  on the photocatalysis was probed, as shown in Fig. S5,† and a volcano relationship was obtained for the photocatalytic  $\text{CO}_2$  reduction performance relative to the Cu content. The  $\text{Cu}_{0.01}/3\text{DOM-TiO}_2$  photocatalyst with a Cu/Ti molar ratio of 1% exhibited optimal performance in both reaction systems. Interestingly, the main product of the photocatalytic  $\text{CO}_2$  reduction reaction in the gas–solid system was  $\text{CH}_4$ , while that in the liquid–solid system was  $\text{C}_2\text{H}_4$  (Fig. S6, ESI†). Fig. 5a shows the time-dependent evolution of  $\text{CH}_4$  and  $\text{CO}$  over the  $\text{Cu}_{0.01}/3\text{DOM-TiO}_2$  photocatalyst in the gas–solid catalytic system, without  $\text{H}_2$  evolution. As a main product,  $\text{CH}_4$  was generated predominately from  $\text{CO}_2$  reduction in the gas–solid catalytic reaction, with a remarkable production rate of  $43.15 \mu\text{mol g}_{\text{cat}}^{-1} \text{h}^{-1}$  and a high selectivity of 83.3% (Fig. 5b). Notably, in the liquid–solid catalytic reaction, the  $\text{Cu}_{0.01}/3\text{DOM-TiO}_2$  photocatalyst exhibits an excellent performance for  $\text{CO}_2$  reduction to  $\text{C}_2\text{H}_4$  (Fig. 5d), accompanied by the generation of  $\text{CO}$  and  $\text{CH}_4$  by-products. The production rate of  $\text{C}_2\text{H}_4$  reaches  $6.99 \mu\text{mol g}_{\text{cat}}^{-1} \text{h}^{-1}$ , with a selectivity of 58.4%, which is of great significance due to the crucial role of  $\text{C}_2\text{H}_4$  in the chemical industry. No liquid product is detected in the reaction solution after 4 h of irradiation (Fig. S7, ESI†). In comparison, the  $\text{Cu}_{0.01}/3\text{DOM-TiO}_2$  photocatalyst presents a higher activity and product selectivity for  $\text{CO}_2$  reduction in the gas–solid catalytic reaction while producing more valuable  $\text{C}_2\text{H}_4$  in the liquid–solid catalytic reaction. These results indicate that the photocatalytic  $\text{CO}_2$  reduction reactions over  $\text{Cu}_{0.01}/3\text{DOM-TiO}_2$  in the two catalytic systems actually follow different reaction pathways. The promotion effects of Cu doping and the 3DOM structure on  $\text{CO}_2$  conversion are testified by the control experiments

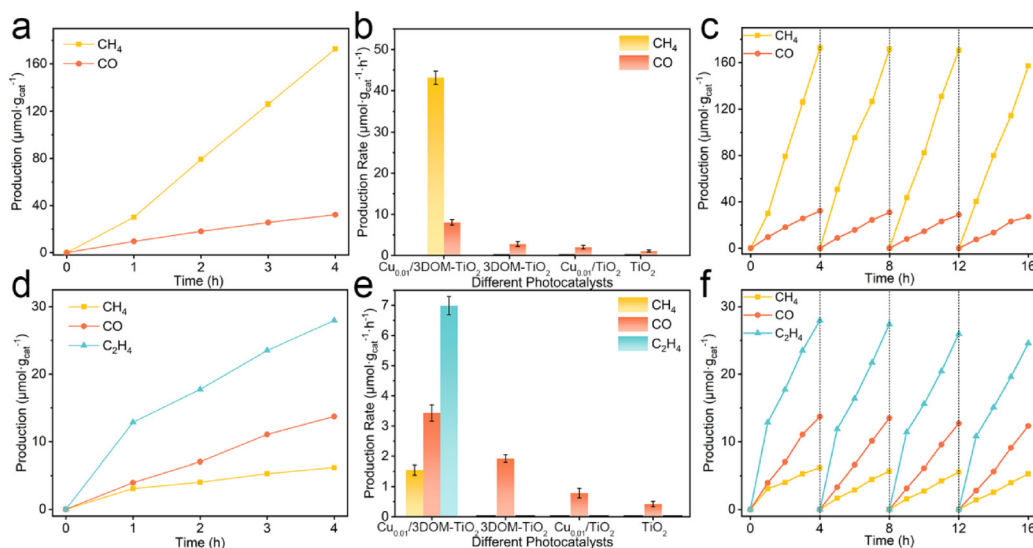


**Fig. 5** Photocatalytic CO<sub>2</sub> reduction performance. (a–c) Gas–solid catalytic reaction: (a) product evolutions over Cu<sub>0.01</sub>/3DOM-TiO<sub>2</sub>, (b) generation rates of products over different photocatalysts, (c) cyclic test of Cu<sub>0.01</sub>/3DOM-TiO<sub>2</sub>. (d–f) Liquid–solid catalytic reaction: (d) product evolutions over Cu<sub>0.01</sub>/3DOM-TiO<sub>2</sub>, (e) generation rates of products over different photocatalysts, (f) cycling test of Cu<sub>0.01</sub>/3DOM-TiO<sub>2</sub>.

of photocatalytic reactions with 3DOM-TiO<sub>2</sub>, Cu<sub>0.01</sub>/TiO<sub>2</sub> and TiO<sub>2</sub>, respectively. As shown in Fig. 5b and e, all the control catalysts without Cu doping or 3DOM structure present very poor photocatalysis toward CO<sub>2</sub> reduction in both the gas–solid and the liquid–solid systems, and none of them has the ability to convert CO<sub>2</sub> into CH<sub>4</sub> or C<sub>2</sub>H<sub>4</sub>, affirming that both Cu single-atom incorporation and the 3DOM structure are crucial for enhancing the photocatalytic CO<sub>2</sub> reduction performance. Subsequently, the durability of the Cu<sub>0.01</sub>/3DOM-TiO<sub>2</sub> photocatalyst was examined by four cycles of the photocatalytic CO<sub>2</sub> reduction reaction with 4 h of irradiation for each cycle in the gas–solid and liquid–solid reaction systems (Fig. 5c and f), respectively. After each cycle, the photocatalyst was exposed to air for recovery. Both the excellent activity and the high selectivity were well maintained after four cycles of the photocatalytic reaction, indicating the good durability of the Cu<sub>0.01</sub>/3DOM-TiO<sub>2</sub> photocatalyst. The XPS analyses (Fig. S8, ESI†) indicate that the surface composition of the Cu<sub>0.01</sub>/3DOM-TiO<sub>2</sub> catalyst remains unchanged after the long-term photocatalytic CO<sub>2</sub> reduction reaction in both the gas–solid and liquid–solid systems, affirming the good stability of the photocatalyst. In addition, several control experiments of the photocatalytic CO<sub>2</sub> reduction reaction were carried out to provide evidence of the CO<sub>2</sub> conversion in both catalytic reaction systems. As shown in Fig. S9 (ESI†), the products are barely generated in the reaction system without CO<sub>2</sub>, light or catalyst, indicating that all the products originate from the photocatalytic CO<sub>2</sub> reduction reaction. When CO<sub>2</sub> is replaced by N<sub>2</sub> in the reaction systems, small amounts of CO and CH<sub>4</sub> are produced at negligible rates over the Cu<sub>0.01</sub>/3DOM-TiO<sub>2</sub> photocatalyst (Fig. S9b and S9d, ESI†), and the production stops after 2 h of irradiation. The slight production of CO and CH<sub>4</sub> can be ascribed to the reduction of surface-adsorbed CO<sub>2</sub> on the photocatalyst by air.

### 3.3. Photocatalytic reaction mechanism

The photoinduced charge transfer from the catalyst to the reactant molecules is critical for photocatalytic reactions. To probe the interfacial charge kinetics, the photocurrent responses of photocatalysts were measured in different atmospheres. The transient photocurrent recorded under an Ar atmosphere is assignable to the electron transfer from catalyst to electrode. Notably, the photocurrent measured in the CO<sub>2</sub>-saturated electrolyte is lower than that measured in the Ar-saturated electrolyte for each photocatalyst (Fig. 6a and b), which is caused by the competitive interfacial electron transfer from the photocatalyst to the surface-adsorbed CO<sub>2</sub> molecules.<sup>61</sup> In comparison, the photocurrents of the Cu-incorporated photocatalysts (Cu<sub>0.01</sub>/3DOM-TiO<sub>2</sub> and Cu<sub>0.01</sub>/TiO<sub>2</sub>) decline more than those of the photocatalysts without Cu (3DOM-TiO<sub>2</sub> and TiO<sub>2</sub>), indicating that the incorporation of Cu is greatly beneficial to the electron transfer from the photocatalyst to the CO<sub>2</sub> molecules. In particular, the Cu<sub>0.01</sub>/3DOM-TiO<sub>2</sub> photocatalyst shows the greatest decrease in photocurrent measured in the CO<sub>2</sub>-saturated electrolyte, corresponding to the most efficient electron delivery from the catalyst to the CO<sub>2</sub> molecules. It is understandable that the high charge separation and transfer efficiencies as well as the favorable CO<sub>2</sub> adsorption ability of the Cu<sub>0.01</sub>/3DOM-TiO<sub>2</sub> photocatalyst jointly contributes to enhancing the electron provision to CO<sub>2</sub> molecules. The significantly enhanced electron transfer efficiency can accelerate the CO<sub>2</sub> activation and the subsequent proton-coupled electron transfer process for hydrocarbon generation.<sup>62</sup> Furthermore, *in situ* ESR detection reveals the generation of radical intermediates during photocatalytic CO<sub>2</sub> reduction with water over the Cu<sub>0.01</sub>/3DOM-TiO<sub>2</sub> catalyst (Fig. 6c). After 10 min of irradiation, the characteristic signal of the carbon-centered radical is obviously

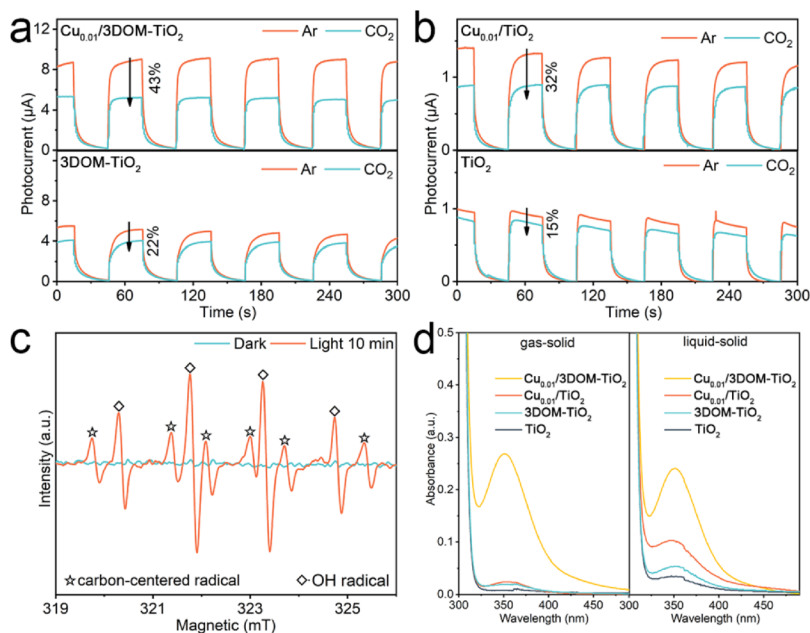


**Fig. 6** (a, b) Transient photocurrents of different catalysts measured in the Ar or CO<sub>2</sub> saturated electrolyte, (c) *in situ* ESR detection of the photocatalytic CO<sub>2</sub> reduction system with Cu<sub>0.01</sub>/3DOM-TiO<sub>2</sub>, (d) UV-vis absorption spectra of the iodometry solution of photocatalytic CO<sub>2</sub> reduction over different photocatalysts in gas-solid and liquid-solid systems.

detected, affirming the activation of chemisorbed CO<sub>2</sub> on the photocatalyst.<sup>63</sup> Meanwhile, the characteristic signal of the hydroxyl radical ( $\cdot\text{OH}$ ) is also observed in the photocatalytic reaction system, which should stem from the oxidation of surface-adsorbed H<sub>2</sub>O molecules by consuming photogenerated holes ( $h^+$ ).<sup>64</sup> Accordingly, hydrogen peroxide (H<sub>2</sub>O<sub>2</sub>) as the product of the oxidation half reaction in both the photocatalytic CO<sub>2</sub> reduction systems is determined by iodometry (Fig. 6d).<sup>65</sup> The H<sub>2</sub>O<sub>2</sub> production rates in gas-solid and liquid-solid reaction systems of the Cu<sub>0.01</sub>/3DOM-TiO<sub>2</sub> photocatalyst are 16.85 and 15.12  $\mu\text{mol g}_{\text{cat}}^{-1} \text{h}^{-1}$ , respectively, which are much higher than those of other photocatalysts (Fig. S10, ESI<sup>†</sup>). The results demonstrate that H<sub>2</sub>O<sub>2</sub> has been produced from the oxidation of surface-adsorbed H<sub>2</sub>O by the photogenerated holes and also confirm the superior activity of the Cu<sub>0.01</sub>/3DOM-TiO<sub>2</sub> photocatalyst toward CO<sub>2</sub> reduction with water.

*In situ* DRIFTS spectra collected from the photocatalytic reaction systems are helpful to identify the surface-bound intermediates of CO<sub>2</sub> transformation and provide crucial clues for understanding the reaction pathway. *In situ* DRIFTS measurements were carried out for both the gas-solid and the liquid-solid catalytic reaction systems under Xe lamp irradiation. In both cases, four broad absorption bands appear in the 3750–3550  $\text{cm}^{-1}$  region (Fig. S11, ESI<sup>†</sup>). The bands centered at 3727 and 3707  $\text{cm}^{-1}$  are attributable to the stretching vibrations of surface-adsorbed -OH groups on Ti<sup>4+</sup> and Ti<sup>3+</sup>, respectively.<sup>66</sup> The bands peaking at 3626 and 3600  $\text{cm}^{-1}$  correspond to the stretching vibrations of O-H in HCO<sub>3</sub><sup>-</sup> and H<sub>2</sub>O, respectively.<sup>67</sup> In comparison, the intensities of the four absorption bands in the liquid-solid catalytic system are much

higher than those of the gas-solid catalytic system due to the water-rich environment of the former. The infrared adsorption signals of the CO<sub>2</sub>-reduction intermediates are displayed in Fig. 7. The peak at 1542  $\text{cm}^{-1}$  in the gas-solid catalytic system is attributable to the surface-bound monodentate carbonate ( $m\text{-CO}_3^{2-}$ ), which is located at 1536  $\text{cm}^{-1}$  for the liquid-solid catalytic system.<sup>68,69</sup> Some infrared adsorption peaks associated with the CO<sub>2</sub> transformation intermediates are obviously detected in both photocatalytic systems. The broad peak at 1448  $\text{cm}^{-1}$  (Fig. 7a) or 1444  $\text{cm}^{-1}$  (Fig. 7b) is ascribed to  $\cdot\text{COOH}$ , a typical one-electron-reduction intermediate.<sup>70</sup> The emergence of the peaks at 1346 and 1559  $\text{cm}^{-1}$  (1350 and 1548  $\text{cm}^{-1}$ ) is indicative of the formation of  $\cdot\text{HCOOH}$  via the protonation process of  $\cdot\text{COOH}$ .<sup>18</sup> The adsorption bands in the region of 1614–1774  $\text{cm}^{-1}$  are assignable to  $\cdot\text{CHO}$ , which is an intermediate generated from  $\cdot\text{HCOOH}$ .<sup>18,71,72</sup> Notably, the infrared signals of the gas-solid catalytic system (Fig. 7a) are much stronger than those of the liquid-solid system (Fig. 7b), due to the higher conversion rate of the former. The low solubility of CO<sub>2</sub> in water restricts the reaction rate of the photocatalytic CO<sub>2</sub> reduction in the liquid-solid system. In addition, several distinctive signals are observed in the *in situ* DRIFTS of both catalytic systems, which provide crucial evidence to reveal the differences in the photocatalytic CO<sub>2</sub> reduction pathways. For the gas-solid catalytic system (Fig. 7a), the sharp peak at 1455  $\text{cm}^{-1}$  appearing after prolonged irradiation is attributed to the  $\cdot\text{CH}_3$  group originating from  $\cdot\text{CHO}$  protonation,<sup>38,73</sup> which is generally considered as a key intermediate for CH<sub>4</sub> production. For the liquid-solid catalytic system (Fig. 7b), the characteristic peak of  $\cdot\text{CH}_3$  is absent, but a new peak at

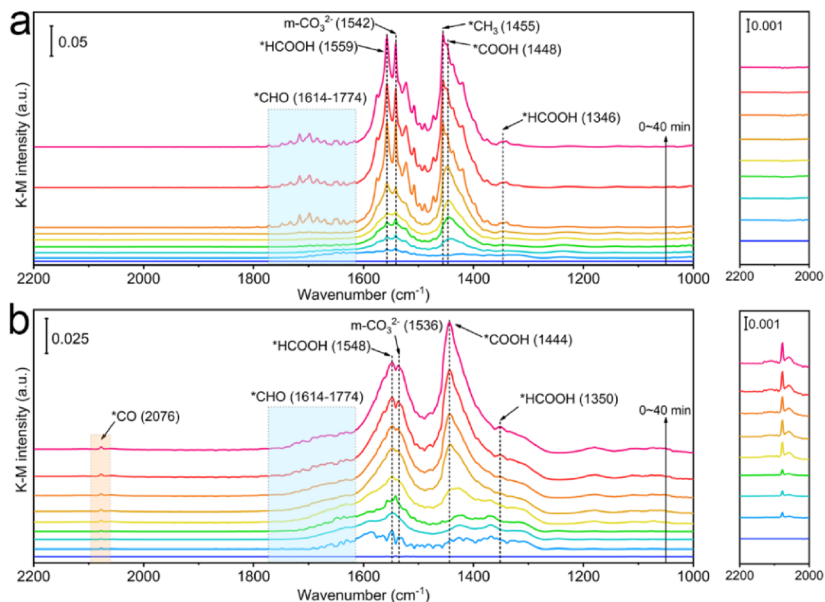


**Fig. 7** *In situ* DRIFTS of the photocatalytic CO<sub>2</sub> reduction with Cu<sub>0.01</sub>/3DOM-TiO<sub>2</sub> catalyst in two different reaction systems: (a) gas–solid catalytic system, (b) liquid–solid catalytic system.

2076 cm<sup>-1</sup> is increasingly apparent with the irradiation, which can be assigned to the chemisorbed \*CO.<sup>70,74</sup> The previous report proved that the intermolecular interaction between surface-adsorbed CO and interfacial water is critical for the formation of ethylene during the electrochemical reduction of CO.<sup>75</sup> The interfacial water is helpful to stabilize the CO dimer, a key intermediate in ethylene formation, by hydrogen bonding to the terminal oxygens of the adsorbed CO molecules. The porous structure of the Cu<sub>0.01</sub>/3DOM-TiO<sub>2</sub> photo-

catalyst provides a water-rich local environment during CO<sub>2</sub> reduction in the liquid–solid system, which is beneficial to the stabilization and dimerization of the \*CO intermediate.<sup>76</sup>

According to the above analyses, the photocatalytic mechanism and possible CO<sub>2</sub> reduction pathways over the Cu<sub>0.01</sub>/3DOM-TiO<sub>2</sub> photocatalyst in two different systems are illustrated in Fig. 8. 3DOM-TiO<sub>2</sub> is excited to generate electron–hole pairs under simulated sunlight, and the photogenerated electrons are efficiently captured by the positively charged Cu<sup>δ+</sup>

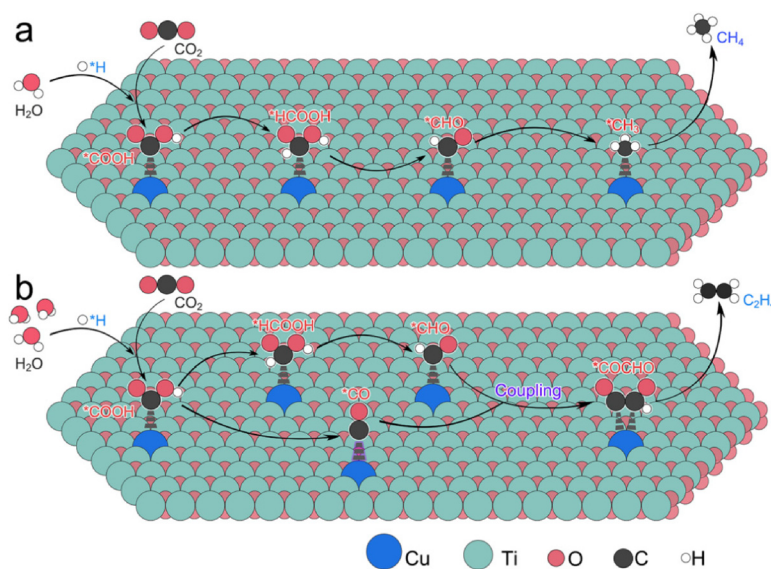
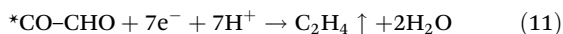
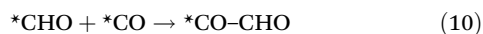
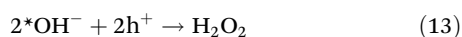
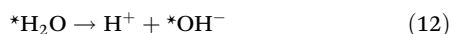


**Fig. 8** The possible mechanisms of photocatalytic CO<sub>2</sub> reduction over Cu<sub>0.01</sub>/3DOM-TiO<sub>2</sub> catalyst in two different reaction systems: (a) gas–solid catalytic system, (b) liquid–solid catalytic system.

( $0 < \delta \leq 2$ ) single-atom sites. The enhanced electron density at Cu sites facilitates the conversion of CO<sub>2</sub> into hydrocarbons (CH<sub>4</sub> or C<sub>2</sub>H<sub>4</sub>) *via* the multi-proton coupled multi-electron reduction process. Specifically, the adsorption and activation of CO<sub>2</sub> molecules are achieved at the Cu<sup>δ+</sup> active sites of photocatalyst, where the adsorbed CO<sub>2</sub> undergoes a continuous hydrogenation process to form \*COOH, followed by the generation of \*HCOOH and \*CHO intermediates. In the gas–solid photocatalytic system (Fig. 8a), CH<sub>4</sub> is produced as the main product *via* the hydrogenation process of \*CHO. On the other hand, it is widely accepted that the generation of the C<sub>2</sub> product undergoes three different reaction paths: (1) a \*COCO intermediate from \*CO dimerization, (2) a \*COCHO intermediate from the dimerization between \*CO and \*CHO, and (3) a \*CHOCHO intermediate from \*CHO dimerization.<sup>71,77,78</sup> In the liquid–solid system of photocatalytic CO<sub>2</sub> reduction (Fig. 8b), the coexistence of \*CO and \*CHO intermediates is a crucial clue to speculate that the formation of C<sub>2</sub>H<sub>4</sub> follows the pathway of the \*COCHO intermediate from dimerization between \*CO and \*CHO. Therefore, the possible reaction pathways of photocatalytic CO<sub>2</sub> reduction in the present gas–solid and liquid–solid systems are described in eqn (1)–(5) and (6)–(11), respectively, where \* denotes the catalytically active sites on the photocatalyst and ↑ represents the release of the gas product.



The oxidation half-reactions in both the catalytic systems are the formation of H<sub>2</sub>O<sub>2</sub> *via* the consumption of photogenerated holes by water (eqn (12) and (13)).



The photocatalytic CO<sub>2</sub> reduction reaction in liquid–solid system is restricted by the low solubility of CO<sub>2</sub> in water (33 mM at 1 atm and 25 °C) and the poor mass transfer of CO<sub>2</sub> in the liquid phase.<sup>79</sup> However, the diffusion coefficient of CO<sub>2</sub> in the gas phase ( $\sim 0.1 \text{ cm}^2 \text{ s}^{-1}$ ) is about 10 000 times that in

the liquid phase ( $\sim 1 \times 10^{-5} \text{ cm}^2 \text{ s}^{-1}$ ), which allows the rapid delivery of CO<sub>2</sub> molecules to the surface of photocatalysts with uncovered active sites. The adsorption and activation of CO<sub>2</sub> and H<sub>2</sub>O can be implemented more efficiently in the gas–solid system, and thus the photocatalyst shows higher activity.

## 4. Conclusion

In summary, the Cu single atom-incorporated 3DOM-TiO<sub>2</sub> photocatalyst was synthesized using a low-cost and mass-production template-assisted pyrolysis strategy and further demonstrated for solar-powered CO<sub>2</sub> conversion into hydrocarbons. The 3DOM structure with large surface area maximizes the exposed sites for anchoring Cu single atoms in a TiO<sub>2</sub> matrix, which enhances the light absorption as well as affording more accessible active sites for CO<sub>2</sub> reduction. The photocatalytic CO<sub>2</sub> reduction with H<sub>2</sub>O was conducted in the gas–solid and liquid–solid systems, respectively, to explore the effects of reaction modes on CO<sub>2</sub> conversion efficiency and product selectivity. The Cu<sub>0.01</sub>/3DOM-TiO<sub>2</sub> photocatalyst exhibits higher activity and selectivity for CH<sub>4</sub> production from CO<sub>2</sub> reduction in the gas–solid system while showing a favorable performance for converting CO<sub>2</sub> to C<sub>2</sub>H<sub>4</sub> in the liquid–solid system. Both the excellent activity and the selectivity are well maintained after a long irradiation time, indicating the good durability of the Cu<sub>0.01</sub>/3DOM-TiO<sub>2</sub> photocatalyst. Compared with the 3DOM-TiO<sub>2</sub>-based photocatalysts reported previously (Table S8, ESI<sup>†</sup>), the Cu<sub>0.01</sub>/3DOM-TiO<sub>2</sub> catalyst exhibits superior photocatalytic CO<sub>2</sub> reduction performance without using any noble metal cocatalysts. The photocatalytic mechanisms in both reaction systems were investigated by *in situ* DRIFTS analyses. It is proposed that CH<sub>4</sub> is generated as the main product *via* the \*CHO intermediate in the gas–solid system while C<sub>2</sub>H<sub>4</sub> is produced *via* the dimerization of \*CO and \*CHO in the liquid–solid system. This work develops a scalable strategy for preparing Cu-SA-incorporated photocatalysts but also offers a new idea for regulating the product selectivity of CO<sub>2</sub> photoreduction by altering the reaction system.

## Author contributions

Cong Chen: methodology, investigation, data curation, visualization, writing – original draft. Ting Wang: methodology, investigation, validation. Ke Yan: investigation, validation. Shoujie Liu: software, data curation. Yu Zhao: software, funding acquisition. Benxia Li: supervision, conceptualization, writing – review & editing, funding acquisition.

## Conflicts of interest

The authors declare no conflict of interest.

## Acknowledgements

This work was supported by the National Natural Science Foundation of China (21471004), the Open Research Fund Program of Key Laboratory of Surface & Interface Science of Polymer Materials of Zhejiang Province (SISPM-2021-02) and the Science Foundation of Zhejiang Sci-Tech University (17062002-Y).

## Notes and references

- X. B. Li, Z. K. Xin, S. G. Xia, X. Y. Gao, C. H. Tung and L. Z. Wu, Semiconductor nanocrystals for small molecule activation via artificial photosynthesis, *Chem. Soc. Rev.*, 2020, **49**, 9028–9056.
- C. Gao and Y. Xiong, Solar-driven artificial carbon cycle, *Chin. J. Chem.*, 2021, **40**, 153–159.
- E. Gong, S. Ali, C. B. Hiragond, H. S. Kim, N. S. Powar, D. Kim, H. Kim and S.-I. In, Solar fuels: Research and development strategies to accelerate photocatalytic CO<sub>2</sub> conversion into hydrocarbon fuels, *Energy Environ. Sci.*, 2022, **15**, 880–937.
- T. Kong, J. Low and Y. Xiong, Catalyst: how material chemistry enables solar-driven CO<sub>2</sub> conversion, *Chem*, 2020, **6**, 1035–1038.
- Z.-H. Xue, D. Luan, H. Zhang and X. W. Lou, Single-atom catalysts for photocatalytic energy conversion, *Joule*, 2022, **6**, 92–133.
- S. Shin, R. Haaring, J. So, Y. Choi and H. Lee, Highly durable heterogeneous atomic catalysts, *Acc. Chem. Res.*, 2022, **55**, 1372–1382.
- L. Zeng and C. Xue, Single metal atom decorated photocatalysts: Progress and challenges, *Nano Res.*, 2020, **14**, 934–944.
- J. Wei, F. L. Meng, T. Li, T. Zhang, S. Xi, W. L. Ong, X. Q. Wang, X. Zhang, M. Bosman and G. W. Ho, Spontaneous atomic sites formation in wurtzite CoO nanorods for robust CO<sub>2</sub> photoreduction, *Adv. Funct. Mater.*, 2021, **32**, 2109693.
- X. Xiong, C. Mao, Z. Yang, Q. Zhang, G. I. N. Waterhouse, L. Gu and T. Zhang, Photocatalytic CO<sub>2</sub> reduction to CO over Ni single atoms supported on defect-rich zirconia, *Adv. Energy Mater.*, 2020, **10**, 2002928.
- Z. Chen, S. Wu, J. Ma, S. Mine, T. Toyao, M. Matsuoka, L. Wang and J. Zhang, Non-oxidative coupling of methane: N-type doping of niobium single atoms in TiO<sub>2</sub>-SiO<sub>2</sub> induces electron localization, *Angew. Chem., Int. Ed.*, 2021, **60**, 11901–11909.
- L. Luo, L. Fu, H. Liu, Y. Xu, J. Xing, C.-R. Chang, D.-Y. Yang and J. Tang, Synergy of Pd atoms and oxygen vacancies on In<sub>2</sub>O<sub>3</sub> for methane conversion under visible light, *Nat. Commun.*, 2022, **13**, 2930.
- S. Ji, Y. Qu, T. Wang, Y. Chen, G. Wang, X. Li, J. Dong, Q. Chen, W. Zhang, Z. Zhang, S. Liang, R. Yu, Y. Wang, D. Wang and Y. Li, Rare-Earth single erbium atoms for enhanced photocatalytic CO<sub>2</sub> reduction, *Angew. Chem., Int. Ed.*, 2020, **59**, 10651–10657.
- S. Ali, A. Razzaq, H. Kim and S.-I. In, Activity, selectivity, and stability of Earth-abundant CuO/Cu<sub>2</sub>O/Cu<sup>0</sup>-based photocatalysts toward CO<sub>2</sub> reduction, *Chem. Eng. J.*, 2022, **429**, 131579.
- Z. Sun, Y. Hu, D. Zhou, M. Sun, S. Wang and W. Chen, Factors influencing the performance of copper-bearing catalysts in the CO<sub>2</sub> reduction system, *ACS Energy Lett.*, 2021, **6**, 3992–4022.
- T. Yang, X. Mao, Y. Zhang, X. Wu, L. Wang, M. Chu, C.-W. Pao, S. Yang, Y. Xu and X. Huang, Coordination tailoring of Cu single sites on C<sub>3</sub>N<sub>4</sub> realizes selective CO<sub>2</sub> hydrogenation at low temperature, *Nat. Commun.*, 2021, **12**, 6022.
- J. Wang, T. Heil, B. Zhu, C.-W. Tung, J. Yu, H. M. Chen, M. Antonietti and S. Cao, A single Cu-center containing enzyme-mimic enabling full photosynthesis under CO<sub>2</sub> reduction, *ACS Nano*, 2020, **14**, 8584–8593.
- H. X. Zhang, Q. L. Hong, J. Li, F. Wang, X. Huang, S. Chen, W. Tu, D. Yu, R. Xu, T. Zhou and J. Zhang, Isolated square-planar copper center in boron imidazolate nanocages for photocatalytic reduction of CO<sub>2</sub> to CO, *Angew. Chem., Int. Ed.*, 2019, **58**, 11752–11756.
- Y. Yu, X. Dong, P. Chen, Q. Geng, H. Wang, J. Li, Y. Zhou and F. Dong, Synergistic effect of Cu single atoms and Au-Cu alloy nanoparticles on TiO<sub>2</sub> for efficient CO<sub>2</sub> photoreduction, *ACS Nano*, 2021, **15**, 14453–14464.
- Y. Zhao, Y. Zhao, R. Shi, B. Wang, G. I. N. Waterhouse, L. Z. Wu, C. H. Tung and T. Zhang, Tuning oxygen vacancies in ultrathin TiO<sub>2</sub> nanosheets to boost photocatalytic nitrogen fixation up to 700 nm, *Adv. Mater.*, 2019, **31**, 1806482.
- Q. Zhao, C. Zhang, R. Hu, Z. Du, J. Gu, Y. Cui, X. Chen, W. Xu, Z. Cheng, S. Li, B. Li, Y. Liu, W. Chen, C. Liu, J. Shang, L. Song and S. Yang, Selective etching quaternary MAX phase toward single atom copper immobilized MXene (Ti<sub>3</sub>C<sub>2</sub>Cl<sub>x</sub>) for efficient CO<sub>2</sub> electroreduction to methanol, *ACS Nano*, 2021, **15**, 4927–4936.
- H. Bao, Y. Qiu, X. Peng, J.-A. Wang, Y. Mi, S. Zhao, X. Liu, Y. Liu, R. Cao, L. Zhuo, J. Ren, J. Sun, J. Luo and X. Sun, Isolated copper single sites for high-performance electroreduction of carbon monoxide to multicarbon products, *Nat. Commun.*, 2021, **12**, 238.
- Y. Zhang, J. Zhao, H. Wang, B. Xiao, W. Zhang, X. Zhao, T. Lv, M. Thangamuthu, J. Zhang, Y. Guo, J. Ma, L. Lin, J. Tang, R. Huang and Q. Liu, Single-atom Cu anchored catalysts for photocatalytic renewable H<sub>2</sub> production with a quantum efficiency of 56%, *Nat. Commun.*, 2022, **13**, 58.
- Y. Zhang, B. Xia, J. Ran, K. Davey and S. Z. Qiao, Atomic-level reactive sites for semiconductor-based photocatalytic CO<sub>2</sub> reduction, *Adv. Energy Mater.*, 2020, **10**, 1903879.
- F. Wen and W. Liu, Three-dimensional ordered macroporous materials for photocatalysis: Design and applications, *J. Mater. Chem. A*, 2021, **9**, 18129–18147.

- 25 A.-Y. Lo and F. Taghipour, Ordered mesoporous photocatalysts for CO<sub>2</sub> photoreduction, *J. Mater. Chem. A*, 2021, **9**, 26430–26453.
- 26 X. Z. Zheng, J. Han, Y. Fu, Y. Deng, Y. Y. Liu, Y. Yang, T. Wang and L. W. Zhang, Highly efficient CO<sub>2</sub> reduction on ordered porous Cu electrode derived from Cu<sub>2</sub>O inverse opals, *Nano Energy*, 2018, **48**, 93–100.
- 27 J. Jiao, Y. Wei, Y. Zhao, Z. Zhao, A. Duan, J. Liu, Y. Pang, J. Li, G. Jiang and Y. Wang, AuPd/3DOM-TiO<sub>2</sub> catalysts for photocatalytic reduction of CO<sub>2</sub>: High efficient separation of photogenerated charge carriers, *Appl. Catal., B*, 2017, **209**, 228–239.
- 28 C. Wang, X. Liu, W. He, Y. Zhao, Y. Wei, J. Xiong, J. Liu, J. Li, W. Song, X. Zhang and Z. Zhao, All-solid-state Z-scheme photocatalysts of g-C<sub>3</sub>N<sub>4</sub>/Pt/macroporous-(TiO<sub>2</sub>@carbon) for selective boosting visible-light-driven conversion of CO<sub>2</sub> to CH<sub>4</sub>, *J. Catal.*, 2020, **389**, 440–449.
- 29 X. Tao, R. Long, D. Wu, Y. Hu, G. Qiu, Z. Qi, B. Li, R. Jiang and Y. Xiong, Anchoring positively charged Pd single atoms in ordered porous ceria to boost catalytic activity and stability in suzuki coupling reactions, *Small*, 2020, **16**, 2001782.
- 30 H. S. Jeon, J. Timoshenko, C. Rettenmaier, A. Herzog, A. Yoon, S. W. Chee, S. Oener, U. Hejral, F. T. Haase and B. R. Cuenya, Selectivity control of Cu nanocrystals in a gas-fed flow cell through CO<sub>2</sub> pulsed electroreduction, *J. Am. Chem. Soc.*, 2021, **143**, 7578–7587.
- 31 J. Fu, K. Jiang, X. Qiu, J. Yu and M. Liu, Product selectivity of photocatalytic CO<sub>2</sub> reduction reactions, *Mater. Today*, 2020, **32**, 222–243.
- 32 Y. C. Tan, K. B. Lee, H. Song and J. Oh, Modulating local CO<sub>2</sub> concentration as a general strategy for enhancing C–C coupling in CO<sub>2</sub> electroreduction, *Joule*, 2020, **4**, 1104–1120.
- 33 X. Wang, P. Ou, J. Wicks, Y. Xie, Y. Wang, J. Li, J. Tam, D. Ren, J. Y. Howe, Z. Wang, A. Ozden, Y. Z. Finfrook, Y. Xu, Y. Li, A. S. Rasouli, K. Bertens, A. H. Ip, M. Graetzel, D. Sinton and E. H. Sargent, Gold-in-copper at low \*CO coverage enables efficient electromethanation of CO<sub>2</sub>, *Nat. Commun.*, 2021, **12**, 3387.
- 34 X. Wang, S. Shen, Z. Feng and C. Li, Time-resolved photoluminescence of anatase/rutile TiO<sub>2</sub> phase junction revealing charge separation dynamics, *Chin. J. Catal.*, 2016, **37**, 2059–2068.
- 35 Q. Xu, Y. Ma, J. Zhang, X. Wang, Z. Feng and C. Li, Enhancing hydrogen production activity and suppressing CO formation from photocatalytic biomass reforming on Pt/TiO<sub>2</sub> by optimizing anatase–rutile phase structure, *J. Catal.*, 2011, **278**, 329–335.
- 36 C. Peng, T. Zhou, P. Wei, H. Ai, B. Zhou, H. Pan, W. Xu, J. Jia, K. Zhang, H. Wang and H. Yu, Regulation of the rutile anatase TiO<sub>2</sub> phase junction *in situ* grown on -OH terminated Ti<sub>3</sub>C<sub>2</sub>T<sub>x</sub> (MXene) towards remarkably enhanced photocatalytic hydrogen evolution, *Chem. Eng. J.*, 2022, **439**, 135685.
- 37 B.-R. Chen, V.-H. Nguyen, J. C. S. Wu, R. Martin and K. Kočí, Production of renewable fuels by the photohydrogenation of CO<sub>2</sub>: effect of the Cu species loaded onto TiO<sub>2</sub> photocatalysts, *Phys. Chem. Chem. Phys.*, 2016, **18**, 4942–4951.
- 38 N. Li, B. Wang, Y. Si, F. Xue, J. Zhou, Y. Lu and M. Liu, Toward high-value hydrocarbon generation by photocatalytic reduction of CO<sub>2</sub> in water vapor, *ACS Catal.*, 2019, **9**, 5590–5602.
- 39 D. Qi, L. Lu, Z. Xi, L. Wang and J. Zhang, Enhanced photocatalytic performance of TiO<sub>2</sub> based on synergistic effect of Ti<sup>3+</sup> self-doping and slow light effect, *Appl. Catal., B*, 2014, **160–161**, 621–628.
- 40 M. Zhang, W. Liao, Y. Wei, C. Wang, Y. Fu, Y. Gao, L. Zhu, W. Zhu and H. Li, Aerobic oxidative desulfurization by nanoporous tungsten oxide with oxygen defects, *ACS Appl. Nano Mater.*, 2021, **4**, 1085–1093.
- 41 S. Wu, Z. Chen, W. Yue, S. Mine, T. Toyao, M. Matsuoka, X. Xi, L. Wang and J. Zhang, Single-atom high-valent Fe(IV) for promoted photocatalytic nitrogen hydrogenation on porous TiO<sub>2</sub>-SiO<sub>2</sub>, *ACS Catal.*, 2021, **11**, 4362–4371.
- 42 Y. Zhang, C. Cao, X.-T. Wu and Q.-L. Zhu, Three-dimensional porous copper-decorated bismuth-based nanofoam for boosting the electrochemical reduction of CO<sub>2</sub> to formate, *Inorg. Chem. Front.*, 2021, **8**, 2461–2467.
- 43 J. A. Benavides, C. P. Trudeau, L. F. Gerlein and S. G. Cloutier, Laser selective photoactivation of amorphous TiO<sub>2</sub> films to anatase and/or rutile crystalline phases, *ACS Appl. Energy Mater.*, 2018, **1**, 3607–3613.
- 44 Z. Luo, A. S. Poyraz, C.-H. Kuo, R. Miao, Y. Meng, S.-Y. Chen, T. Jiang, C. Wenos and S. L. Suib, Crystalline mixed phase (anatase/rutile) mesoporous titanium dioxides for visible light photocatalytic activity, *Chem. Mater.*, 2014, **27**, 6–17.
- 45 Y. Ma, X. Yi, S. Wang, T. Li, B. Tan, C. Chen, T. Majima, E. R. Waclawik, H. Zhu and J. Wang, Selective photocatalytic CO<sub>2</sub> reduction in aerobic environment by microporous Pd-porphyrin-based polymers coated hollow TiO<sub>2</sub>, *Nat. Commun.*, 2022, **13**, 1400.
- 46 S. Jiang, K. Zhao, M. Al-Mamun, Y. L. Zhong, P. Liu, H. Yin, L. Jiang, S. Lowe, J. Qi, R. Yu, D. Wang and H. Zhao, Design of three-dimensional hierarchical TiO<sub>2</sub>/SrTiO<sub>3</sub> heterostructures towards selective CO<sub>2</sub> photoreduction, *Inorg. Chem. Front.*, 2019, **6**, 1667–1674.
- 47 T. Wu, X. Zhu, Z. Xing, S. Mou, C. Li, Y. Qiao, Q. Liu, Y. Luo, X. Shi, Y. Zhang and X. Sun, Greatly improving electrochemical N<sub>2</sub> reduction over TiO<sub>2</sub> nanoparticles by Iron doping, *Angew. Chem., Int. Ed.*, 2019, **58**, 18449–18453.
- 48 J. Y. Do, R. K. Chava, K. K. Mandari, N.-K. Park, H.-J. Ryu, M. W. Seo, D. Lee, T. S. Senthil and M. Kang, Selective methane production from visible-light-driven photocatalytic carbon dioxide reduction using the surface plasmon resonance effect of superfine silver nanoparticles anchored on lithium titanium dioxide nanocubes (Ag@Li<sub>x</sub>TiO<sub>2</sub>), *Appl. Catal., B*, 2018, **237**, 895–910.

- 49 M. Xiao, L. Zhang, B. Luo, M. Lyu, Z. Wang, H. Huang, S. Wang, A. Du and L. Wang, Molten-salt-mediated synthesis of an atomic nickel Co-catalyst on TiO<sub>2</sub> for improved photocatalytic H<sub>2</sub> evolution, *Angew. Chem., Int. Ed.*, 2020, **59**, 7230–7234.
- 50 Z. Wang, X. Mao, P. Chen, M. Xiao, S. A. Monny, S. Wang, M. Konarova, A. Du and L. Wang, Understanding the roles of oxygen vacancies in hematite-based photoelectrochemical processes, *Angew. Chem., Int. Ed.*, 2019, **58**, 1030–1034.
- 51 C. Liu, Y. Qin, W. Guo, Y. Shi, Z. Wang, Y. Yu and L. Wu, Visible-light-driven photocatalysis over nano-TiO<sub>2</sub> with different morphologies: From morphology through active site to photocatalytic performance, *Appl. Surf. Sci.*, 2022, **580**, 152262.
- 52 G. Wang, C.-T. He, R. Huang, J. Mao, D. Wang and Y. Li, Photoinduction of Cu single atoms decorated on UiO-66-NH<sub>2</sub> for enhanced photocatalytic reduction of CO<sub>2</sub> to liquid fuels, *J. Am. Chem. Soc.*, 2020, **142**, 19339–19345.
- 53 J. Yang, X. Zhu, Z. Mo, J. Yi, J. Yan, J. Deng, Y. Xu, Y. She, J. Qian, H. Xu and H. Li, A multidimensional In<sub>2</sub>S<sub>3</sub>-CuInS<sub>2</sub> heterostructure for photocatalytic carbon dioxide reduction, *Inorg. Chem. Front.*, 2018, **5**, 3163–3169.
- 54 J. Y. Do, N. Son, R. K. Chava, K. K. Mandari, S. Pandey, V. Kumaravel, T. S. Senthil, S. W. Joo and M. Kang, Plasmon-induced hot electron amplification and effective charge separation by Au nanoparticles sandwiched between copper titanium phosphate nanosheets and improved carbon dioxide conversion to methane, *ACS Sustainable Chem. Eng.*, 2020, **8**, 18646–18660.
- 55 A. A. Liu, L. C. Liu, Y. Cao, J. M. Wang, R. Si, F. Gao and L. Dong, Controlling dynamic structural transformation of atomically dispersed CuO<sub>x</sub> species and influence on their catalytic performances, *ACS Catal.*, 2019, **9**, 9840–9851.
- 56 Y. Wang, Z. Chen, P. Han, Y. Du, Z. Gu, X. Xu and G. Zheng, Single-atomic Cu with multiple oxygen vacancies on ceria for electrocatalytic CO<sub>2</sub> reduction to CH<sub>4</sub>, *ACS Catal.*, 2018, **8**, 7113–7119.
- 57 B.-H. Lee, S. Park, M. Kim, A. K. Sinha, S. C. Lee, E. Jung, W. J. Chang, K.-S. Lee, J. H. Kim, S.-P. Cho, H. Kim, K. T. Nam and T. Hyeon, Reversible and cooperative photoactivation of single-atom Cu/TiO<sub>2</sub> photocatalysts, *Nat. Mater.*, 2019, **18**, 620–626.
- 58 Z. Xu, C. Guo, X. Liu, L. Li, L. Wang, H. Xu, D. Zhang, C. Li, Q. Li and W. Wang, Ag nanoparticles anchored organic/inorganic Z-Scheme 3DOMM-TiO<sub>2</sub>-based heterojunction for efficient photocatalytic and photoelectrochemical water splitting, *Chin. J. Catal.*, 2022, **43**, 1360–1370.
- 59 X. Lv, D. Y. S. Yan, F. L.-Y. Lam, Y. H. Ng, S. Yin and A. K. An, Solvothermal synthesis of copper-doped BiOBr microflowers with enhanced adsorption and visible-light driven photocatalytic degradation of norfloxacin, *Chem. Eng. J.*, 2020, **401**, 126012.
- 60 R. K. Chava, J. Y. Do and M. Kang, Enhanced photoexcited carrier separation in CdS-SnS<sub>2</sub> heteronanostructures: A new 1D-0D visible-light photocatalytic system for the hydrogen evolution reaction, *J. Mater. Chem. A*, 2019, **7**, 13614–13628.
- 61 N. Zhang, A. Jalil, D. Wu, S. Chen, Y. Liu, C. Gao, W. Ye, Z. Qi, H. Ju, C. Wang, X. Wu, L. Song, J. Zhu and Y. Xiong, Refining defect states in W<sub>18</sub>O<sub>49</sub> by Mo doping: A strategy for tuning N<sub>2</sub> activation towards solar-driven nitrogen fixation, *J. Am. Chem. Soc.*, 2018, **140**, 9434–9443.
- 62 X. Chang, T. Wang and J. Gong, CO<sub>2</sub> photo-reduction: Insights into CO<sub>2</sub> activation and reaction on surfaces of photocatalysts, *Energy Environ. Sci.*, 2016, **9**, 2177–2196.
- 63 S. Kreft, R. Schoch, J. Schneidewind, J. Rabeah, E. V. Kondratenko, V. A. Kondratenko, H. Junge, M. Bauer, S. Wohlrab and M. Beller, Improving selectivity and activity of CO<sub>2</sub> reduction photocatalysts with oxygen, *Chem*, 2019, **5**, 1818–1833.
- 64 Y. Nosaka and A. Nosaka, Understanding hydroxyl radical (<sup>•</sup>OH) generation processes in photocatalysis, *ACS Energy Lett.*, 2016, **1**, 356–359.
- 65 Z. Tian, C. Han, Y. Zhao, W. Dai, X. Lian, Y. Wang, Y. Zheng, Y. Shi, X. Pan, Z. Huang, H. Li and W. Chen, Efficient photocatalytic hydrogen peroxide generation coupled with selective benzylamine oxidation over defective ZrS<sub>3</sub> nanobelts, *Nat. Commun.*, 2021, **12**, 2039.
- 66 R. Long, Y. Li, Y. Liu, S. Chen, X. Zheng, C. Gao, C. He, N. Chen, Z. Qi, L. Song, J. Jiang, J. Zhu and Y. Xiong, Isolation of Cu atoms in Pd lattice: Forming highly selective sites for photocatalytic conversion of CO<sub>2</sub> to CH<sub>4</sub>, *J. Am. Chem. Soc.*, 2017, **139**, 4486–4492.
- 67 Ş. Neaţu, J. A. Maciá-Agulló, P. Concepción and H. Garcia, Gold-copper nanoalloys supported on TiO<sub>2</sub> as photocatalysts for CO<sub>2</sub> reduction by water, *J. Am. Chem. Soc.*, 2014, **136**, 15969–15976.
- 68 Y. Huang, K. Li, J. Zhou, J. Guan, F. Zhu, K. Wang, M. Liu, W. Chen and N. Li, Nitrogen-stabilized oxygen vacancies in TiO<sub>2</sub> for site-selective loading of Pt and CoO<sub>x</sub> cocatalysts toward enhanced photoreduction of CO<sub>2</sub> to CH<sub>4</sub>, *Chem. Eng. J.*, 2022, **439**, 135744.
- 69 W. He, Y. Wei, J. Xiong, Z. Tang, W. Song, J. Liu and Z. Zhao, Insight into reaction pathways of CO<sub>2</sub> photoreduction into CH<sub>4</sub> over hollow microsphere Bi<sub>2</sub>MoO<sub>6</sub>-supported Au catalysts, *Chem. Eng. J.*, 2022, **433**, 133540.
- 70 W. Wang, C. Deng, S. Xie, Y. Li, W. Zhang, H. Sheng, C. Chen and J. Zhao, Photocatalytic C–C coupling from carbon dioxide reduction on copper oxide with mixed-valence copper(I)/copper(II), *J. Am. Chem. Soc.*, 2021, **143**, 2984–2993.
- 71 W. Ma, S. Xie, T. Liu, Q. Fan, J. Ye, F. Sun, Z. Jiang, Q. Zhang, J. Cheng and Y. Wang, Electrocatalytic reduction of CO<sub>2</sub> to ethylene and ethanol through hydrogen-assisted C–C coupling over fluorine-modified copper, *Nat. Catal.*, 2020, **3**, 478–487.
- 72 B. N. Choi, J. Y. Seo, Z. An, P. J. Yoo and C.-H. Chung, An *in situ* spectroscopic study on the photochemical CO<sub>2</sub> reduction on CsPbBr<sub>3</sub> perovskite catalysts embedded in a porous copper scaffold, *Chem. Eng. J.*, 2022, **430**, 132807.

- 73 R. Zhang, H. Wang, S. Tang, C. Liu, F. Dong, H. Yue and B. Liang, Photocatalytic oxidative dehydrogenation of ethane using CO<sub>2</sub> as a soft oxidant over Pd/TiO<sub>2</sub> catalysts to C<sub>2</sub>H<sub>4</sub> and syngas, *ACS Catal.*, 2018, **8**, 9280–9286.
- 74 M. Wang, M. Shen, X. Jin, J. Tian, M. Li, Y. Zhou, L. Zhang, Y. Li and J. Shi, Oxygen vacancy generation and stabilization in CeO<sub>2-x</sub> by Cu introduction with improved CO<sub>2</sub> photocatalytic reduction activity, *ACS Catal.*, 2019, **9**, 4573–4581.
- 75 J. Li, X. Li, C. M. Gunathunge and M. M. Waegele, Hydrogen bonding steers the product selectivity of electrocatalytic CO reduction, *Proc. Natl. Acad. Sci. U. S. A.*, 2019, **116**, 9220–9229.
- 76 P. B. Joshi, N. Karki and A. J. Wilson, Electrocatalytic CO<sub>2</sub> reduction in acetonitrile enhanced by the local environment and mass transport of H<sub>2</sub>O, *ACS Energy Lett.*, 2022, **7**, 602–609.
- 77 J. X. Hao, D. Yang, J. J. Wu, B. X. Ni, L. J. Wei, Q. J. Xu, Y. L. Min and H. X. Li, Utilizing new metal phase nanocomposites deep photocatalytic conversion of CO<sub>2</sub> to C<sub>2</sub>H<sub>4</sub>, *Chem. Eng. J.*, 2021, **423**, 130190.
- 78 L. Hou, J. Han, C. Wang, Y. Zhang, Y. Wang, Z. Bai, Y. Gu, Y. Gao and X. Yan, Ag nanoparticle embedded Cu nanoporous hybrid arrays for the selective electrocatalytic reduction of CO<sub>2</sub> towards ethylene, *Inorg. Chem. Front.*, 2020, **7**, 2097–2106.
- 79 H. Huang, R. Shi, Z. Li, J. Zhao, C. Su and T. Zhang, Triphase photocatalytic CO<sub>2</sub> reduction over silver-decorated titanium oxide at a gas–water boundary, *Angew. Chem.*, 2022, **61**, e202200802.